Dichotomous impact of afferent sensory noise on grid-patterned firing and path integration in a continuous attractor network model

Harshith Nagaraj and Rishikesh Narayanan*

Cellular Neurophysiology Laboratory, Molecular Biophysics Unit, Indian Institute of Science, Bangalore 560012, India

***Corresponding Author**

Rishikesh Narayanan
Molecular Biophysics Unit
Indian Institute of Science
Bangalore 560 012, India.

e-mail: rishi@iisc.ac.in
Phone: +91-80-22933372
Fax: +91-80-23600535

ACKNOWLEDGMENTS

The authors thank members of the cellular neurophysiology laboratory for helpful discussions through the project and for comments on a draft of this manuscript. This work was supported by the Wellcome Trust-DBT India Alliance (Senior fellowship to R. N.; IA/S/16/2/502727) and the Kishore Vaigyanik Protsahan Yojana (H. N.).

AUTHOR CONTRIBUTIONS

H. N. and R. N. designed experiments; H. N. performed experiments; H. N. analyzed data; H. N. and R. N. wrote the paper.

COMPETING INTEREST STATEMENT

The authors declare that they have no competing interests.

ABSTRACT

Background: The continuous attractor network (CAN) model has been effective in explaining grid-patterned firing in the rodent medial entorhinal cortex, with strong lines of experimental evidence and widespread utilities in understanding spatial navigation and path integration. A surprising lacuna in CAN analyses is the paucity of quantitative studies on the impact of afferent sensory noise on path integration. Here, we evaluate the impact of afferent sensory noise on grid-patterned firing and on the accuracy of position estimates derived from network pattern flow velocity. Motivated by the ability of border cells to act as an error-correction mechanism, we also assess the impact of interaction between afferent noise and border cell inputs on CAN performance.

Methodology: We used an established 2D CAN model that received velocity inputs from a virtual animal traversing a 2D arena to generate grid-patterned firing. We estimated network pattern flow velocity from network activity and used that to compute an activity-based position estimate at each time step. We tracked the difference between the real and the estimated positions as a function of time and called it the deviation in integrated path (DIP). We defined afferent sensory noise to be additive Gaussian, with different noise levels achieved by changing the variance. We introduced north and east border cells and connected them to grid cells based on co-activity patterns. For different levels of noise, we computed DIP and metrics for grid-patterned activity in the presence *vs*. absence of border cells. Importantly, to avoid potential bias owing to the use of a single trajectory in computing these measurements, we performed all simulations across 50 different trajectories.

Results: The computed grid scores and position accuracy (as DIP) showed pronounced trajectory-to-trajectory variability, even in a noise-free network. With the introduction of sensory noise, the variability prevailed and unveiled a dichotomous impact of afferent sensory noise on position accuracy *vs*. grid-patterned activity. Specifically, low levels of sensory noise improved position estimation accuracy without altering the ability of the network to generate grid-patterned activity. In contrast, high levels of sensory noise impaired position estimates as well as grid-patterned activity, although position estimates were more sensitive to sensory noise compared to grid-patterned activity. The stochastic resonance observed in the relationship between position accuracy and sensory noise level was partially explained by the interaction of noisy inputs with the rectification nonlinearity in the neural transfer function. Finally, across noise levels, pronounced trajectory-to-trajectory variability in grid-score and position accuracy was observed with the addition of border inputs. Across the population of trajectories, addition of border inputs yielded modest changes in both measurements across noise levels.

Implications: Our analyses demonstrate that the robustness of grid-patterned activity in CAN models to noise does not extend to other functions of the CAN model. Stochastic resonance with reference to position estimation and sensory noise implies that biological CANs could evolve to yield optimal performance (path integration) in the presence of noise in biological sensory systems. An important methodological implication that emerges from our observations is the critical need to account for trajectory-to-trajectory variability in position estimates and path integration. Given the pronounced nature of trajectory-to-trajectory variability, conclusions based on a single trajectory are bound to be erroneous thereby warranting analyses with multiple trajectories. Together, our analyses unveil important roles for sensory noise in improving position estimates obtained from activity in CAN models.

INTRODUCTION

The theory of path integration is one of the influential theories used to explain the phenomenon of spatial navigation, a behavior crucial to the survival of most organisms. The path integration theory relies on the tracking of self-motion and iterative updation of an internal coordinate to track the position. The continuous attractor network (CAN) forms one of the widely used frameworks that can implement path integration. Here, a network of neurons embedded with strong recurrent connectivity, coupled with asymmetry in the form of head-direction preferences 'integrate' self-motion inputs to represent different spatial locations in the form of different activity states (Samsonovich & McNaughton, 1997; Fuhs & Touretzky, 2006; Burak & Fiete, 2009; Savelli & Knierim, 2019; Khona & Fiete, 2022; Dong & Fiete, 2024). The model explains the formation of grid cells, which are cells that have spatial firing fields which follow a hexagonal firing pattern (Hafting *et al.*, 2005). There are lines of evidence that support the toroidal nature of connectivity employed by most versions of the model (Gardner *et al.*, 2022; Khona & Fiete, 2022; Dong & Fiete, 2024).

Modeling studies have incorporated empirical observations such as phase precession and theta-dependence in grid cell networks (Hasselmo & Brandon, 2012; Navratilova *et al.*, 2012; Bush & Burgess, 2014), intrinsic theta resonance as well as heterogeneities in intrinsic properties and synaptic connectivity (Mittal & Narayanan, 2021), after-spike dynamics (Navratilova *et al.*, 2012), and stochastic spiking (Burak & Fiete, 2009) to examine the impact grid cell networks and their stability. However, these studies feed deterministic self-motion inputs to the system, thereby precluding analyses of the impact of variability in velocity inputs on network performance. Given the ubiquitous nature of noise in biological systems in general and sensory systems in particular (Faisal *et al.*, 2008), in this study, we address the impact of introducing sensory noise in the afferent inputs to the continuous attractor network. We asked if the introduction of sensory noise would (a) affect the ability of the network to yield stable grid-fields; and (b) alter the ability of the network to accurately track the position of the animal. We used a well-studied 2D CAN model to address these questions through separate quantitative metrics to assess grid-cell stability and the efficacy of path integration.

We found that the ability of the continuous attractor network to yield grid fields was extremely robust to the addition of sensory noise, with stable grid fields formed across a range of afferent noise levels. Grid cell activity was disrupted only at extremely high levels of noise. In striking contrast, we found the manifestation of stochastic resonance in the impact of afferent sensory noise on the efficiency of path integration. Specifically, we continually tracked the

position of the virtual animal using shift in network activity and computed deviation in the integrated path for networks receiving different levels of afferent noise. We surprisingly found that low levels of noise reduced deviation in integrated path, while higher noise levels were detrimental to the efficacy of path integration. These observations indicate that low levels of sensory noise might be beneficial to a CAN model performing path integration. Probing the mechanistic basis for such stochastic resonance, we traced the origins to the nonlinearities in the neural transfer function and how they shaped the activity lobes within each grid field. Specifically, we found that low levels of noise enhanced detection of sub-threshold sensory signals, which in turn enhanced the ability of the resultant activity patterns to enhance accuracy of estimated location. On the other hand, with high levels of noise, the dominance of noise over the velocity signal degraded efficient path integration, together yield an optimal level of noise that yielded minimal error in path integration.

The dichotomy between the impact of afferent sensory noise on grid-cell stability and path integration in the same network motivated us to probe if dichotomies were prevalent with other external inputs to the grid-cell network. In addition, we also asked if the presence of other external inputs would alleviate the deleterious impact of high levels of afferent noise on path integration. Several studies have posited that external inputs in the form of border cell inputs can lead to stabilization of grid fields and reduction in path-integration error by recalibrating the system (Cheung *et al.*, 2012; Hardcastle *et al.*, 2015; Giocomo, 2016; Pollock *et al.*, 2018). Motivated by these, we examined the effect of introducing border cell inputs, as either inhibitory or excitatory external inputs to the network, on network performance at various levels of afferent noise. We found that introducing borders did not yield qualitative difference in terms of grid-field formation across noise levels. However, in certain scenarios, the presence of border cell inputs resulted in quantitative increases in grid scores. With reference to path integration, border inputs did not enhance the ability of network activity to predict position at low noise levels but led to modest enhancement in prediction when noise levels were high.

Together, our results unveil the dichotomy of grid cell networks in eliciting grid-patterned activity *vs.* in estimating external position from network activity. While grid-patterned activity was extremely robust to the presence of afferent sensory noise, position estimation manifested stochastic resonance with increasing levels of sensory noise. Our results also showed that the addition of border inputs to the network was not sufficient to improve system performance with high levels of noise. Our analyses also unveil trajectory-to-trajectory variability in position estimate evolution, emphasizing the need for multi-trajectory analyses in assessing path integration in CAN models.

RESULTS

The goal of this study was to assess the impact of afferent sensory noise and additional afferent inputs (in the form of border cells) on CAN performance using different quantitative metrics. We implemented a rate-based CAN model made of a 2D neural sheet (60 × 60 = 3600 neurons) built with integrator neurons (Burak & Fiete, 2009). The neural sheet was endowed with periodic boundary conditions resulting in a toroidal configuration. Each neuron in the network received two sets of synaptic inputs: (i) a feedforward afferent sensory input which was dependent on the velocity of the virtual animal; and (ii) all-inhibitory recurrent inputs from other neurons within the neural sheet with a location-dependent connectivity. We introduced afferent sensory noise to the feedforward input as a zero-mean Gaussian-distributed additive component, whose variance determined the level of noise. The movement of the virtual animal was modeled to occur in a square arena (2 m × 2 m). We implemented a modified version of the virtual trajectory used by (Mittal & Narayanan, 2021) in order to optimize computational costs required to fully cover the arena (see Methods for details).

Robustness of grid-patterned activity to afferent sensory noise.

Existing analyses of grid-cell CAN models do not account for the presence of noise in the afferent inputs to the network, which is ubiquitous across all sensory modalities. Would incorporation of stochasticity in afferent inputs affect the ability of the continuous attractor network to yield stable grid-cell like patterns? How robust is the network to the addition of noise to afferent sensory inputs? To address these questions, we introduced noise in the afferent inputs to the 2D CAN in the form of an additive Gaussian of zero mean and variable standard deviation (σ_η). The standard deviation of the Gaussian was varied to yield 5 different levels of noise (L1–L5) with L0 denoting the deterministic case where no noise was introduced. Neural activity was recorded as a virtual animal traversed the square arena following a virtual trajectory. The activity map of the 3600 neurons in the network as a function of 2D space within the arena was computed with the same virtual trajectory, but with different levels of noise.

Example patterns of activity across the arena for two different grid cells with different levels of noise showed that grid-patterned activity was remarkably robust to the addition of noise (Fig. 1*A*). To quantify this across all neurons in the network, we computed grid score for each neuron in network. The grid scores (Fig. 1*B*) and other grid-field measurements (Supplementary Fig. S1*A*–*G*) confirmed the remarkable robustness of grid-patterned firing to the addition of sensory noise. Specifically, we found stable grid-fields across most noise levels,

with the manifestation of instability limited to the highest level of noise (Fig. 1; Supplementary Fig. S1). The design of virtual trajectory was such that the mean velocity of the animal during the run (μ_v) was 3×10^{-3} m per time step (1 ms). The remarkable nature of the robustness of spatially patterned firing to noise might be discerned by noting that stable grid patterns were observed even when the ratio σ_η/μ_v exceeded 1. The disruption in grid-patterned firing occurred at L5 level of noise where σ_η/μ_v was greater than 5.

Sensory noise-driven stochastic resonance in the accuracy of position estimated from network pattern flow velocity.

How does the presence of afferent noise affect the relationship between the network pattern flow velocity and the velocity of the virtual animal? How does the estimate of animal position obtained from the network pattern flow velocity compare with the actual position as a function of time? To characterize the ability of network pattern flow velocity to track animal position and to assess the impact of noise on the accuracy of the position estimate, we defined *deviation in integrated path*, $D_{IP}(t)$. $D_{IP}(t)$ was computed over a period of 1 s for all time points t, as the average squared difference between the position estimate (obtained from the network pattern flow velocity) and the real position of the virtual animal in the arena. $D_{IP}(t)$ represented the accuracy with which we can estimate the animal's position using the network pattern flow velocity and track this as the virtual animal traverses the arena. Quantitatively, a lower value of D_{IP} indicated enhanced accuracy in the position estimate obtained from network activity.

In computing D_{IP}, we estimated network pattern flow velocity from the difference maps of network activity obtained at two consecutive time points (Fig. 2*A*). We identified the centroids of the adjacent positive and negative lobes associated with each grid field in the difference map by computing the centroids of independent convex hulls for the two lobes (Fig. 2*A*). The lines connecting the two centroids (associated with positive and negative lobes of a given grid field in the difference map), computed across all grid fields, provided an estimate of network pattern flow velocity at each time point. We scaled the network pattern flow velocity to arrive at a velocity estimate of the animal ($\vec{\boldsymbol{v}}_{net}$) and compared it with the actual velocity of the animal ($\vec{\boldsymbol{v}}_{real}$). We found $\vec{\boldsymbol{v}}_{net}$ and $\vec{\boldsymbol{v}}_{real}$ to be highly correlated (Fig. 2*C*). In the network that lacked sensory noise (L0 level), with a given virtual trajectory, we found D_{IP} to initially increase as a function of time but to eventually settle down at a low level of deviation (Fig. 2*D*). For a single trajectory, we observed that with addition of noise paradoxically resulted in an *increase* in the accuracy of the position estimate of the animal obtained using the network

velocity. Specifically, compared to L0 noise level, we noticed a reduction in D_{IP} across most timepoints for the L1 and L2 levels of noise, whereas L3 and L4 levels of noise resulted in an increase in D_{IP} across most timepoints (Fig. 3*A*). We could not quantify the deviation for L5 levels of noise due to our inability to construct the convex hull (Supplementary Fig. 1*H*) owing to the absence of well-defined grid fields (Fig. 1). As the identification of convex hulls is an essential requirement for estimating position from network activity, we were unable to compute D_{IP} for L5 noise levels.

As the specific values of D_{IP} could be reflective of the specific virtual trajectory employed, we repeated our analyses with 50 different virtual trajectories and computed the deviation (Fig. 3*B*–*C*) as well as grid score (Fig. 3*D*) for each of the 50 runs. Strikingly, we found that the mean deviation obtained for noise levels L1 and L2 was consistently lower than the mean deviation for the noise-free level L0 (Fig. 3*B*). However, for L3 and L4, the deviation was higher compared to the other three levels of noise. These results demonstrated that a low level of afferent sensory noise (L1–L2) significantly improved position estimates of the CAN model across different trajectories compared to no-noise conditions (Fig. 3*C*). In contrast, high levels of sensory noise (L3–L4) significantly degraded position estimates (Fig. 3*C*). The ability of an optimal level of noise to improve system performance, with performance dropping on either side of the optimal noise level, has been referred to as stochastic resonance (McDonnell & Abbott, 2009). Together, these results unveiled the manifestation of stochastic resonance in the accuracy of position estimates obtained from network activity with reference to the variance of afferent sensory noise.

An important observation about the need for performing simulations with multiple trajectories emerged from trajectory-to-trajectory variability that we observed in the quantitative metrics across different trajectories for the same network. Specifically, pronounced variability in D_{IP} (Fig. 3*C*) and average grid scores (Fig. 3*D*) across different trajectories strongly emphasized the need to validate network performance with multiple trajectories, even in noise-free conditions (*e.g.*, L0 variability in Figs. 3*C*–*D*). If analyses were performed with a single trajectory, the biases associated with that single trajectory drives the conclusions. For instance, stochastic resonance observed in the deviation measurement (Fig. 3*B*) would not have been evident it analyses relied on a single trajectory (Fig. 3*A*) and the biases associated with that single trajectory. It required multiple runs to eliminate the trajectory-driven biases to actually assess the impact of sensory noise on this measurement.

Importantly, this noise-induced enhancement in estimation accuracy was not associated with changes in mean grid scores computed from the 50 different trajectories (Fig. 3*D*). Specifically, mean grid scores computed for L1–L2 noise levels were not significantly different from those computed for L0 noise levels across the 50 different trajectories (Fig. 3*D*). Together, these results (Figs. 1–3) demonstrated a dichotomy in the impact of afferent sensory noise on position estimation accuracy *vs*. grid-patterned activity generation in a continuous attractor network. Low levels of sensory noise improved position estimation accuracy without altering the ability of the network in generating grid-patterned activity. In contrast, high levels of sensory noise impaired position estimates as well as grid-patterned activity, although position estimates were more sensitive to sensory noise compared to grid-patterned activity (Figs. 1–3).

Progressive reduction in mean hull separation with increase in sensory noise variance contributes to dependence of position estimate on sensory noise.

What was the basis for the enhanced position estimates obtained with the low levels of noise? To address this question, we revisited the process by which we compute the network pattern flow velocity and how neural activity is related to all inputs (including noisy velocity inputs). The central step in the estimation of network pattern flow velocity is the vector connecting the centroids of the convex hulls constructed for the maxima and minima of the activity difference map (Fig. 2*B*). Therefore, we first assessed the impact of afferent noise on this distance (the magnitude of the vector connecting the two convex hulls) and referred to this as hull separation. We computed the distribution of mean hull separation (across all grid fields) at each time point for the same trajectory with different levels of sensory noise. We found that increases in noise level resulted in a reduction in mean hull separation, manifesting as a progressive leftward shift in the cumulative distribution of mean hull separation with increasing noise level (Fig. 4*A*).

Animal position is estimated from the estimated animal velocity from network activity ($\vec{\boldsymbol{v}}_{net}$), which depends on the hull separation vector. A reduction in hull separation for the same values of real velocity ($\vec{\boldsymbol{v}}_{real}$) values implies that there'd be differences in the animal velocity estimated from network activity. To quantify this, we computed error in velocity estimate (Δv) as the magnitude of the difference between $\vec{\boldsymbol{v}}_{real}$ and $\vec{\boldsymbol{v}}_{net}$ ($\Delta \mathrm{v} = \|(\vec{\boldsymbol{v}}_{real} - \vec{\boldsymbol{v}}_{net})\|$) at each time point for the same trajectory with different levels of sensory noise. Owing to the reduction in the hull separation, we observed that the error in velocity estimate was higher in case of L3 and L4 levels of noise compared to the noise-free scenario (Fig. 4*B*). Notably, we observed that the error in velocity estimates for the noise-free L0 level was slightly higher than the L1 level of

noise pointing to hull separation as one potential source for the stochastic resonance observed in D_{IP} (Fig. 3).

Thus, based on these observations, we propose a model which reconciles the reduction in mean hull separation and the stochastic resonance in D_{IP} with addition of sensory noise (Fig. 4*C*). In the absence of sensory noise, the mean hull separation is large, which results in an overestimate of the animal velocity. This overestimate manifests as a relatively high value of Δv (Fig. 4*B*), resulting in high deviation at zero noise conditions. With increasing noise levels, the mean hull separation progressively reduces (Fig. 4*A*). At an optimal level of low levels of noise, the estimated velocity approaches the real value thus ceasing to be an overestimate, together leading to a reduction in D_{IP} (Fig. 3). Upon further increase in the noise level, the mean hull separation is reduced further (Fig. 4*B*), yielding an underestimate of the real velocity. This manifests as increased error in velocity estimate (Fig. 4*C*) and a higher value of D_{IP} (Fig. 3).

The distribution of inputs to the rectifying nonlinearity in individual neurons is a key factor contributing to network estimates of position.

What factors contributed to the reduction in hull separation that we had observed with increase in noise (Fig. 4*A*)? We noted that the rectifying nonlinearity in individual neurons contributes to the conversion total inputs to neural activity at every time point. We reasoned that increase in noise would enhance the range of the overall inputs arriving onto individual neurons, thus resulting in higher activity in the presence of noise. This higher activity could result in expansion of the lobes at each time point, together yielding a reduction in hull separation. To test this, we recorded inputs onto each neuron in the network across all time points for the same trajectory with different levels of noise. We plotted the distribution of these inputs and found that the input range indeed increased with increasing noise (Fig. 4*D*). Together, these observations indicated that noise-induced enhancement in range of inputs in conjunction with the rectification resulted in an ability to detect inputs that were sub-zero under no-noise conditions. This enhancement resulted in a reduction in hull separation with increased noise.

If noise were indeed operating through an enhancement in the range of inputs that are converted to neural activity, then alterations to the range of positive inputs *under noise-free conditions* should yield have same effects as noise on hull separation and network-based estimates. To test this, we modified the neural activation function to involve a non-zero threshold for rectification. Specifically, the neural activation function was of the form:

$$f(x) = \begin{cases} x: & x > \varepsilon \\ 0: & \text{otherwise} \end{cases}$$

The default value of ε was zero, setting up a rectification that is true to the input. To alter the extent of positive inputs to the neuron, we changed ε to either positive or negative number. Whereas a negative ε enhances input range as more negative values would now contribute to neural activity (compared to $\varepsilon = 0$), a positive ε reduces the input range. Thus, if our hypothesis on the link between input range and hull separation were true, then a progressive negative shift in ε should reduce the hull separation. We obtained hull separation, velocity estimates, and average deviation values for networks with different values of ε with the same trajectory in the absence of noise (Fig. 5). Consistent with our hypothesis, we found that a more negative value for ε resulted in a reduction in hull separation (Fig. 5*A*), an increase in the error of estimated velocity (Fig. 5*B*), and an enhancement in deviation (Fig. 5*C*). We noticed that shifts obtained with changes in ε (Fig. 5*A*) were not as large as those obtained with changes in noise variance (Fig. 4*A*). In addition, we did not observe an enhancement in velocity or position estimates because of shifting the hull separation (Fig. 5*B*–*C*) suggesting that noise-induced stochastic resonance wasn't simply an effect of hull separation.

Together, our analyses with variable rectification threshold values confirmed a relationship between average deviation and input range to neurons that was in accordance with our proposed model assessing the impact of noise variance. However, unlike the impact of noise, the altered threshold did not enhance performance. These observations suggest that the enhancement observed at lower noise levels are not due to an increase in the extent of input range but could be because of noise-induced detection of sub-threshold inputs without alteration to the threshold.

Addition of border inputs did not affect the path integration accuracy of the system.

Border cell inputs are known to serve as an error-correcting mechanism for grid cells (Hardcastle *et al.*, 2015) and serve to minimize the drift in grid patterns over time (Pollock *et al.*, 2018). Motivated by this, we asked if the addition of border inputs could increase the accuracy of the position estimate obtained using the network activity in the presence of afferent sensory noise. We introduced border inputs to grid cells using two different types of connectivity: (i) an inhibitory pattern, wherein grid cells coactive with border cells received lower levels of inhibition; (ii) and an excitatory pattern, wherein grid cells coactive with border cells received higher levels of excitation. The connectivity pattern was constructed using grid cell co-activity during a representative run and used for later runs to introduce border cells.

Two border cells were considered to provide inputs to grid cells: one that fired along the north border and another along the east border, to potentially serve as corrective influences along orthogonal directions (Fig. 6*A*).

For a single trajectory run of simulations, we computed grid-cell metrics for each of the 3600 in the absence of noise and found that the addition of border inputs (through excitatory or inhibitory connectivity) had a modest impact on these metrics (Supplementary Fig. S2). Specifically, we observed modest changes in grid score (increase), firing rate (increase), peak firing rate (increase), information rate (increase), mean field size (reduction), average spacing (reduction), and sparsity (reduction) (Supplementary Fig. S2). To avoid biases associated with the use of a single trajectory, we performed network simulations with border cells over the 50 different trajectories used earlier and with different levels of noise. The modest increase that we observed in grid score with a single-trajectory run did not hold when we repeated our analyses for 50 different trajectories in the absence of noise (Fig. 6*B*). Specifically, in noise-free networks, the mean grid scores obtained across the 50 different trajectories were statistically comparable irrespective of whether border inputs (through excitatory or inhibitory inputs) were present or not (Fig. 6*B*; L0). The pronounced trajectory-to-trajectory variability in mean grid scores even in noise-free simulations (Fig. 6*B*; L0) further emphasized the need to use multiple trajectories to avoid trajectory-driven biases in conclusions drawn from such network simulations.

With the addition of noise, the trajectory-to-trajectory variability continued to manifest, with significant increase in mean grid score observed only when inhibitory borders were introduced at noise level L4 (Fig. 6*B*). Grid score for the rest the noise levels were statistically comparable. For the highest level of noise, grid-patterned firing was lost across all networks irrespective of whether border cells were present or absent (Fig. 6*B*; L5). Together, these observations showed that the 2D CAN network was inherently robust in generating grid-patterned activity but manifested pronounced trajectory-to-trajectory variability in grid score values. The addition of border inputs showed modest improvement in grid score values for certain levels of noise, but the network was statistically comparable in terms of their grid scores across different trajectories for most scenarios.

We next turned to accuracy of location estimation in the presence of border cells. We repeated our analyses with 50 trajectories for different levels of noise (from Fig. 3*C*) in the presence of border inputs, implemented either through excitatory or inhibitory connectivity (Fig. 7). We had earlier (Fig. 3*C*) established that the presence of low levels of noise enhanced location estimates manifesting as a reduction in the deviation metric D_{IP} for L1–L2 levels of

noise, but increased values of D_{IP} for L3–L4 levels (all compared to noise-free L0). Under noise-free conditions, the estimation accuracy was statistically comparable irrespective of whether border inputs were present or not (Fig. 7*A*). Strikingly, with low levels of noise (L1–L2), D_{IP} measured across 50 trajectories was slightly higher (significantly so for L2) when border inputs were present. In contrast, with increase in noise level (L3–L4), border inputs slightly enhanced the estimation accuracy in the presence of border inputs (significantly so for L4, inhibitory connectivity). Consistent with these modest changes in position estimates with the introduction of border inputs, we also found that each of hull separation, velocity estimation error, and pre-rectification input distribution showed modest changes with introduction of border inputs (Supplementary Fig. S3). Overall, similar to what we observed for grid scores across the population of trajectories, the impact of border inputs on position estimation was modest across noise levels and across both kinds of connectivity.

Together, our results showed that introduction of border inputs introduced modest differences in grid score and position measurements across different levels of noise. These observations emphasize the need to account for trajectory-to-trajectory variability in assessment of metrics associated with the grid-cell network. They also show that the introduction of border inputs was not sufficient to alleviate the deleterious impact of high levels of noise on location estimates.

DISCUSSION

The principal goal of this study was to assess the impact of introducing sensory noise in the afferent inputs to the CAN model on grid-fields and the ability of the network to track position. Our analyses demonstrate the robustness of the grid-firing fields generated by the model to sensory noise, with disruption in patterns observed at extreme levels of noise. In striking contrast to this robustness, we report the manifestation of stochastic resonance with reference to accuracy of position estimated from network activity in the presence of sensory noise. Specifically, whereas low levels of noise were beneficial in estimating the animal position with greater accuracy, high levels of noise were detrimental. Finally, we found that introduction of border cell inputs to the grid cell network had modest impact on grid-patterned activity or on position estimation.

Robustness of the grid patterns to sensory noise.

Noise is ubiquitous in biological systems across all scales. Sources of noise in biological systems include stochasticity in ion-channel opening, synaptic release, binding of molecules involved in signaling cascades, which can propagate across scales to introduce widespread variability in responses (Faisal *et al.*, 2008; Ribrault *et al.*, 2011). Thus, the fundamental requirement for a biological system is to maintain its functionality in the presence of such stochasticity. With reference to CAN models, although the impact of noise in neural spiking has been assessed (Burak & Fiete, 2009), the impact of sensory noise at the input end of the neurons has not been assessed. Our observations on the stability of grid-patterned firing patterns over a wide range of noise levels demonstrate the extent of robustness exhibited by the CAN model. Such robustness in pattern generation is expected from a network exhibiting attractor dynamics, wherein the specific connectivity patterns and stable activity propagation across the neural sheet counteracts the perturbations induced by noise (Cannon *et al.*, 1983; Khona & Fiete, 2022). The presence of multiple 'activity bumps' in the neural sheet also has been shown to contribute to robustness to noise (Wang & Kang, 2022). Our observations on robustness of grid-patterned firing to a wide range of afferent noise is therefore consistent with prior observations and is a reason for the attractiveness of the framework for patterned activity generation.

Stochastic resonance in the ability to estimate position accurately using network activity. Stochastic resonance has been observed in neural systems across scales, ranging from molecules to single neurons to perceptual levels (Douglass *et al.*, 1993; Collins *et al.*, 1995b, a; Gluckman *et al.*, 1996; Moss, 1997; Simonotto *et al.*, 1997; Russell *et al.*, 1999; Mittal & Narayanan, 2022). Our analyses shows that the remarkable robustness of grid-patterned firing in CAN models doesn't extend to accuracy of position estimates from neural activity. Specifically, our analyses demonstrate the beneficial effect of low levels of noise in estimating the position accurately using network activity, with higher levels of noise resulting in reduced accuracy despite robustness in grid-patterned firing. The manifestation of stochastic resonance implies that a biological CAN could evolve in the presence of sensory noise, such that optimal path integration is achieved at the specific level of noise that is prevalent in the system. Although we were able to partially explain the reason behind this stochastic resonance using the rectification nonlinearity in the neural activation function, further analyses are required to fully elucidate the underlying mechanisms.

Modest impact of introducing border cell inputs: need to account for multiple trajectories.

Path integration within the CAN framework relies on the iterative update of an internal coordinate by tracking self-motion cues. Drift in position estimates have been shown to accumulate iteratively under such a framework. While studies have relied on border-cell inputs to act as 'corrective influences' under such a scenario (Hardcastle *et al.*, 2015; Giocomo, 2016; Pollock *et al.*, 2018), our results on the effect of borders on the accuracy of the position estimate using network activity under different noise conditions yields an important insight about variability. Irrespective of whether the network received border inputs or not, we observed pronounced trajectory-to-trajectory variability across all measurements. It was therefore essential to compute each measurement across multiple trajectories to avoid biases that are introduced using a single trajectory. With specific reference to path integration and temporally continuous position estimates, the exact nature of each trajectory would result in different errors as a function of time. To study the impact of another variable, such as sensory noise variance or border-cell inputs, on path integration performance, it becomes essential that the dependence of error evolution on individual trajectories are eliminated. Without such elimination, the outcomes are biased by the specific dynamics of that single trajectory thereby providing incorrect inferences. Our analyses demonstrate that the impact of sensory noise (Fig.

3*B*–*D*) or border inputs (Fig. 6–7) on network performance showed wide trajectory-to-trajectory variability and inferences about the new variable were decipherable only across 50 different trajectories. Future studies should study the source of trajectory-to-trajectory variability and how they affect the impact of specific variables on overall network performance using different metrics that probe the varied functions.

Future directions and model limitations.

Our study employs a rate-based model of a continuous attractor network, which is endowed with noisy sensory inputs as well as border inputs to generate grid-patterned activity as well as to estimate position using network activity. Rate-based models are limited in their ability to account for temporal characteristics of spike timings as well as the relationship to the phase of extracellular oscillations (such as the theta oscillation), which are necessary for the spatial selectivity of grid cell activity (Brandon *et al.*, 2011). Future studies expand our analyses using spiking or biophysical neural models that are endowed with other forms of noise including synaptic and channel noise.

Our model employs a homogeneous population of neurons, whereby each neuron possesses similar intrinsic properties and is endowed with similar connectivity patterns. Biological systems, however, are endowed with significant heterogeneity in their properties. Therefore, key questions that need to be addressed are as follows. How would the interplay between the heterogeneity in synaptic and intrinsic properties and sensory noise affect different aspects of the network performance? Could the network maintain robustness in grid-patterned firing across noise even when heterogeneities are introduced? Would the system exhibit stochastic resonance even when such heterogeneities are present?

In the context of heterogeneities in CAN models (Mittal & Narayanan, 2021), neuronal resonance has been shown to serve as a stabilizing mechanism for heterogeneous CAN models (Mittal & Narayanan, 2021). Neuronal resonance is mediated by ion-channel conductances that introduce a slow negative feedback loop (Hutcheon & Yarom, 2000; Mittal & Narayanan, 2021; Mishra & Narayanan, 2023; Mittal & Narayanan, 2024). There are several lines of evidence to support the occurrence of resonance in neurons in the medial entorhinal cortex (Haas & White, 2002; Erchova *et al.*, 2004; Giocomo *et al.*, 2007; Canto & Witter, 2012; Pastoll *et al.*, 2012; Mittal & Narayanan, 2022). Future studies could therefore explore the possibility of whether intrinsic neuronal resonance might suppress the deleterious impact of noise through such a negative feedback loop. In addition, the slow time constants of these

resonating conductances could also increase the time over which neurons could integrate self-motion inputs, which might also lead to an increase in accuracy in position estimate. Since navigation under realistic scenarios involves cluttered regions with several obstacles, object/landmark inputs from the lateral entorhinal cortex (Deshmukh & Knierim, 2011, 2013; Edvardsen *et al.*, 2020) could be explored as an additional corrective influence.

Lastly, we incorporated sensory noise in our model and observed the occurrence of stochastic resonance in network performance. However, we incorporated additive white noise sources in our model, and there are studies that demonstrate that the color of noise plays a critical role as well (Hänggi *et al.*, 1993; Gingl *et al.*, 1995; Nozaki & Yamamoto, 1998; Nozaki *et al.*, 1999). Thus, future studies could look to examine the effect of changing the color of the noise or introducing multiplicative noise could alter the outcomes observed in our model.

METHODS

Development of virtual trajectory.

To reduce computational cost, we modified an algorithm that yields virtual rodent movement (Mittal & Narayanan, 2021) to yield faster trajectories in square arena (2 m × 2 m):

- The starting position of the animal was set to be the center of the arena (x_0 = 1, y_0 = 1).
- For each time step (= 1 ms), the heading direction (ϕ_t) as well as the distance run (d_t) were picked randomly. Thus, the position of the rat at time t, (x_t, y_t) was given by:

$$x_t = x_{t-1} + d_t \cos(\phi_t)$$
$$y_t = y_{t-1} + d_t \sin(\phi_t)$$

  where (x_{t-1}, y_{t-1}) represented the position at the previous time step $t-1$. If (x_t, y_t) exceeded the bounds of the arena, they were computed until a random repick of ϕ_t and d_t allowed the coordinates to fall within the arena.
- To make the virtual trajectory more realistic, the range over which the heading direction (ϕ_t) and distance run (d_t) were picked varied near the boundaries compared to the rest of the arena. To account for the fact that the virtual animal makes fast and sharp turns near the boundaries, the range for ϕ_t was [0, 2π] and d_t range was [0.002, 0.004] m. These ranges were modified to $\phi_t \in$ [–π/36, π/36] and $d_t \in$ [0.0029, 0.0031] away from the borders, to achieve smooth runs with relatively uniform speed.

The range of distances per time step (0.002–0.004 m or 0.0029–0.0031 m) and the value of the integration time step (1 ms) implied that the range of velocity was 2–4 or 2.9–3.1 m/s. This implied an average velocity (μ_v) of the virtual animal at 3 m/s across the arena. We generated 50 virtual trajectories, with different virtual trajectories achieved by altering the seed values of the random number generators used for generating ϕ_t and d_t. These virtual trajectories offered better control over simulation periods and better efficacy in covering the entire arena in short time spans.

Structure and dynamics of the continuous attractor network.

The continuous attractor model used here was adapted from a previous study (Burak & Fiete, 2009). We used a network of 3600 neurons, which were arranged in a 60 × 60 lattice. The network had periodic boundary conditions, which led to a toroidal arrangement. The neurons in the network were modeled as integrators, with a membrane time constant τ_m (default value: 10 ms). Each neuron had a preferred direction θ_i, implying that they received inputs from specific head-direction cells. θ_i could take one of four different values: 0, π/2, π and 3π/2 which

representing the directions east, north, west, and south respectively. The network was divided into local blocks of 2 × 2 cells representing each of these directions (the directional preference of each cell was picked randomly). Thus, one-fourth of the total number of cells in the network preferred a particular direction.

Each neuron in the model received two sets of inputs: an intra-network recurrent inputs from other neurons in the 2D neural sheet and feed-forward inputs that carried information on animal velocity and head-direction preference. The intra-network connectivity followed a shifted Mexican-hat connectivity pattern, which was achieved as a difference of Gaussians, given by (Burak & Fiete, 2009):

$$W_{ij} = W_0\left(x_i - \boldsymbol{x}_j - l\hat{e}_{\theta_j}\right)$$

$$W_0(\boldsymbol{x}) = a\exp(-\gamma|\boldsymbol{x}|^2) - \exp(-\beta|\boldsymbol{x}|^2)$$

$$\beta = \frac{3}{\lambda^2}, \gamma = 1.25 \times \beta$$

where, W_{ij} represented the synaptic weight from the neuron located at $\boldsymbol{x}_j$ to the neuron located at $\boldsymbol{x}_i$ and $\hat{\boldsymbol{e}}_{\theta_j}$ depicted the unit vector pointing along the θ_j direction. The parameter a regulates the synaptic weights, and was set to a default value of 1, which would represent an all-inhibitory network. The parameters β, λ (default value: 13), and γ defined the periodicity of the lattice, while the parameter l (default value: 2) defined the shift along $\hat{\boldsymbol{e}}_{\theta_j}$, and is necessary for the motion of the activity bump consequent to velocity inputs.

The second set of inputs were feed-forward velocity inputs (based on head direction preference) and were excitatory in nature. These were of the form:

$$B_i = 1 + \alpha\hat{\boldsymbol{e}}_{\theta_i}.\vec{\boldsymbol{v}}$$

where, α (default value: 45) denoted the velocity gain, with $\vec{\boldsymbol{v}}$ representing the velocity vector derived from the virtual trajectory of the animal.

The dynamics of each of the 3600 rate-based integrator neurons was governed by:

$$\tau_m\frac{dS_i}{dt} + S_i = f\left(\sum_j W_{ij} + B_i\right)$$

where $f(x)$ represented the neural transfer function as a simple rectification non-linearity ($f(x) = \max(x, \varepsilon)$; $\varepsilon = 0$), and $S_i(t)$ denoted the activity of neuron i at time t. The models were initialized with randomized values of S_i for all neurons with $S_i^0 \in [0,1]$. For the initial 100 ms, a constant feed-forward drive was provided to the network by ensuring velocity input was zero, and this resulted in the spontaneous emergence of a stable pattern. The time step (dt)

was 1 ms and activity patterns were recorded at each time step. For visualization purposes, a spike threshold of 0.1 (a.u.) on S_i was used.

Introduction of afferent sensory noise.

We incorporated sensory noise into the system in the form an additive perturbation η_t^i to the velocity vector $\vec{v}$ for each cell i at each time step t. Thus, the feed-forward input to a neuron i was now given by:

$$B_i = 1 + \alpha \hat{e}_{\theta_i} . \left(\vec{v} + \eta_t^i\right)$$

where η_t^i was picked from a Gaussian distribution with zero mean and standard deviation σ_η. The six levels of noise (L0–L5) were achieved by varying σ_η = 0, 1×10^{-3}, 2×10^{-3}, 3×10^{-3}, 5×10^{-3}, and 1×10^{-2} (L0–L5, in that order).

Quantitative analysis of grid cell activity.

To quantitatively assess the impact of sensory noise on grid-cell activity, we used the following set of standard measurements of grid-cell activity (Fyhn *et al.*, 2004; Hafting *et al.*, 2005; Mittal & Narayanan, 2021). To quantify the rate maps of grid-cell activity in the network, we first divided the arena into 100 × 100 pixels. *Activity spatial maps* were constructed for each cell by taking the activity of the cell at each time and assigning the activity the cell to the specific (x, y) location of the animal in the arena at that time point. *Occupancy spatial maps* were constructed by computing the probability (p_m) of finding the animal in the mth pixel as the fraction of time spent by the animal in the corresponding pixel. *Spatial rate maps* for each cell were computed by normalizing the respective activity spatial map with the occupancy spatial map for that run. These maps were smoothened using a 2D Gaussian filter of standard deviation of 4 pixels. *Average firing rate* (μ) was computed by summing the activity of all the pixels from the spatial rate map and dividing the quantity by the total number of pixels (10,000). *Peak firing rate* ($f_{\max}$) denoted the highest activity value observed in the spatial rate map.

To identify grid fields, all local maxima in the smoothened spatial rate map were detected and individual fields were identified as contiguous regions around the local maxima, with a spatial spread of at least 20% activity relative to the local maxima. The *number of grid fields* was computed as the total number of local peaks detected in the spatial rate map of each cell. The *mean size* of each field was estimated by calculating the ratio between total number of pixels covered by all grid fields to the number of grid fields. The *average spacing* between

grid fields was the ratio of the sum of distances between the local maxima to the total number of distance values.

Grid score was computed by assessing the rotational symmetry of the spatial rate maps. For each neuron, the spatial auto correlation (SAC_{ϕ}) was computed between the spatial rate map and the map rotated by $\phi°$ for $\phi \in [30, 60, 90, 120, 150]$. These values were used to obtain the grid score as follows:

$$Grid\ score = \min(SAC_{60}, SAC_{120}) - \max\,(SAC_{30}, SAC_{90}, SAC_{150})$$

Spatial information rate (I_s) in bits per second was calculated as:

$$I_s = \sum_m p_m \mu_m \log_2\left(\frac{\mu_m}{\mu}\right)$$

where, p_m defined the probability of finding the animal in the mth pixel, μ_m denoted the mean firing rate of the cell in the mth pixel and μ was the average firing rate of the grid cell. *Sparsity* was computed as:

$$Sparsity = \frac{\mu^2}{\sum_i p_i \mu_i^2}$$

where, μ_i represents the mean firing rate of the cell in the ith pixel, and p_i represents the probability of finding the animal in the ith pixel. A lower value of sparsity indicates that the grid-fields are spatially denser.

Quantitative analysis of path integration.

To arrive at a quantitative estimate of path integration, we attempted to arrive at an estimate of the current location of the animal based on network activity. To do this, we first computed the *activity difference map*, defined as the difference between the network activity (activity of each of the 3600 neurons represented as a 60×60 matrix) at time $(t + 1)$ and time t. This is equivalent to computing the differential of the network activity and would yield the 'shift' in network activity between time t and $(t + 1)$. The activity difference map was smoothed with a 2D Gaussian filter with a standard deviation of 1. We estimated the locations of the maxima and minima of the activity difference map, with the maxima denoting cells more active at time $(t + 1)$ compared to time t, while the minima denoted the cells more active at time t compared to time $(t + 1)$. Since these local extrema formed clusters (representing the 'shift' in a particular activity bump), independent convex hulls were identified around each local maxima and the local minima. The positions of the centroid for each hull were then computed for all local maxima and minima. The differences between the centroids of the adjacent local

maximum and the corresponding local minimum were computed for each pair. These differences were averaged across pairs at each time point to give a measure of the network pattern flow velocity for that time point (Fig. 1*C*).

The network pattern flow velocity (computed from the average shift in network activity) would be proportional to the corresponding velocity input to the network ($\vec{\boldsymbol{v}}_{real}$) at each time point. The linear fit between the average shift and $\vec{\boldsymbol{v}}_{real}$ was computed across all timepoints. The average shift was then scaled by the slope of the linear fit to yield the estimate of velocity using the network activity ($\vec{\boldsymbol{v}}_{net}$). In other words, $\vec{\boldsymbol{v}}_{net}$ was obtained by scaling the network pattern flow velocity whereas $\vec{\boldsymbol{v}}_{real}$ depicted the velocity of the virtual animal in the arena. We computed $\vec{\boldsymbol{v}}_{net}$ for all time points after 100 ms (as the velocity input was zero for 100 ms for the spontaneous emergence of stable activity patterns).

As the initial position of the animal at 100 ms was known ($x_{100} = x_0 = 1; y_{100} = y_0 = 1$), we computed the position estimate of the animal (x_t^{net}, y_t^{net})) $\forall$ t > 100 ms using $\vec{\boldsymbol{v}}_{net}$ as:

$$x_t^{net} = x_{t-1}^{net} + v_{net,x}^t$$

$$y_t^{net} = y_{t-1}^{net} + v_{net,y}^t$$

Note that (x_t^{net}, y_t^{net}) is an *estimate* of the position of the animal computed using network activity. This estimate could be different from (x_t, y_t), the *actual* position of the animal based on the virtual trajectory. To quantify the difference between the position estimate obtained using network activity (x_t^{net}, y_t^{net}) and the actual position (x_t, y_t), we defined *deviation in integrated path*, D_{IP} as follows:

$$D_{IP}(t) = \sqrt{\frac{1}{1000}\left[\sum_{t'=t-1000}^{t'=t} \left(x_{t'}^{net} - x_{t'}\right)^2 + \left(y_{t'}^{net} - y_{t'}\right)^2\right]}$$

In words, D_{IP} was computed as the square-root of the sum of the average squared-difference in the *x* and *y* coordinates over a period of 1 s, computed for all time points. The square term ensured sign-independence while the average over 1 s minimized the effect of transient fluctuations. Thus, D_{IP} provided a quantitative measure of the accuracy with which we can estimate the position of the animal using its network activity.

Introduction of border cell inputs.

A border cell was defined as a cell which manifested high activity exclusively near the border of the arena. We incorporated two different border cell inputs, with high activity either near the north border or along the east border. We chose the two border cell inputs in this fashion,

with the hypothesis that the north border cell would correct for errors along the y direction whereas the east border cell would correct for errors along the x direction. This formulation enabled a scenario where we could examine the impact of border cells with the introduction of a minimal number of additional inputs, apart from providing control over the sign (excitatory *vs*. inhibitory) and magnitude of inputs arriving through these additional border cells to the grid cell network. The spatial firing pattern of the north (B_N) and the east (B_E) border cells were defined as follows:

$$B_N = \begin{cases} 1: & y \in [1.9,2] \\ 0: & otherwise \end{cases}$$

$$B_E = \begin{cases} 1: & x \in [1.9,2] \\ 0: & otherwise \end{cases}$$

We noted that this formulation for border cell firing to be within 10 cm close to the border is consistent with the firing pattern of border cells observed empirically (Savelli *et al.*, 2008; Solstad *et al.*, 2008) and with previous computational studies (Hardcastle *et al.*, 2015).

While previous studies have used experience-dependent Hebbian learning to construct the weights of border cell inputs to grid cells (Pollock *et al.*, 2018), we adopt the approach used by (Hardcastle *et al.*, 2015) wherein we assume the presence of mature connections between border and grid cells. Specifically, we use network activity obtained from one of the virtual trajectories to construct the connectivity map between border and grid cells. We constructed two different types of connectivity maps between border and grid cells using this process as follows:

- **Excitatory connectivity:** Considering R_d ($d \in \{N, E\}$) to denote the region over which the border cell B_d was active, we defined the strength of connection between the border cell B_d and a grid cell i (W_{id}) to be proportional to the sum of the activity of the grid cell i over the region R_d:

$$W_{id} = \frac{1}{N_d} \sum_{\vec{x} \in R_d} S_i(\vec{\boldsymbol{x}})$$

  where, $S_i(\vec{\boldsymbol{x}})$ represented the activity of grid cell i at position $\vec{\boldsymbol{x}}$ and N_d was a scaling factor (default value: 10,000). The scaling factor was set such that the strength of border-to-grid connectivity was comparable to the strength of the Mexican hat connectivity. This formulation yielded excitatory connectivity, whereby grid cells that were active over the region where the border cell was active received excitatory connections from the border cell. Grid cells that were coactive with the border cells received excitatory inputs from border cells with the strength of excitation directly related to the level of co-activation.

- **Inhibitory connectivity:** For inhibitory connectivity, W_{id} was defined (with the same notations as above) as:

$$W_{id} = -\left(0.05 - \frac{1}{N_d}\sum_{\vec{x}\in R_d} S_i(\vec{x})\right)$$

  With this formulations, the connections between the border cells and the grid cells are inhibitory in nature. The grid cells that were active over the region R_d received less inhibition compared to grid cells that were not active in the region R_d. In other words, all grid cells received inhibition from border cells, but grid cells that were co-active with border cells received reduced inhibition. The magnitude of reduction in inhibition was directly dependent on the level of co-activation.

With the introduction of border cell inputs, the dynamics of the individual cells of the continuous attractor network was modified as:

$$\tau_m \frac{dS_i}{dt} + S_i = f\left(\sum_j W_{ij}S_j + \sum_{d\in\{N,E\}} W_{id}B_d + B_i\right)$$

with the additional term involving B_d representing the two border cell inputs.

Computational details.

All simulations were performed in MATLAB 2021a (Mathworks Inc, USA) with a simulation step size of 1 ms. All data analyses and plotting were performed using custom-written software within the IGOR Pro (Wavemetrics, USA) or MATLAB environments. All statistical analyses were performed using the R statistical package (http://www.r-project.org/). To avoid false interpretations and to emphasize heterogeneities in simulation outcomes, the entire range of measurements are reported in figures rather than providing only summary statistics (Mittal & Narayanan, 2021).

REFERENCES

Brandon MP, Bogaard AR, Libby CP, Connerney MA, Gupta K & Hasselmo ME. (2011). Reduction of theta rhythm dissociates grid cell spatial periodicity from directional tuning. *Science* **332,** 595-599.

Burak Y & Fiete IR. (2009). Accurate path integration in continuous attractor network models of grid cells. *PLoS computational biology* **5,** e1000291.

Bush D & Burgess N. (2014). A hybrid oscillatory interference/continuous attractor network model of grid cell firing. *J Neurosci* **34,** 5065-5079.

Cannon SC, Robinson DA & Shamma S. (1983). A proposed neural network for the integrator of the oculomotor system. *Biol Cybern* **49,** 127-136.

Canto CB & Witter MP. (2012). Cellular properties of principal neurons in the rat entorhinal cortex. II. The medial entorhinal cortex. *Hippocampus* **22,** 1277-1299.

Cheung A, Ball D, Milford M, Wyeth G & Wiles J. (2012). Maintaining a cognitive map in darkness: the need to fuse boundary knowledge with path integration. *PLoS Comput Biol* **8,** e1002651.

Collins JJ, Chow CC & Imhoff TT. (1995a). Aperiodic stochastic resonance in excitable systems. *Phys Rev E Stat Phys Plasmas Fluids Relat Interdiscip Topics* **52,** R3321-R3324.

Collins JJ, Chow CC & Imhoff TT. (1995b). Stochastic resonance without tuning. *Nature* **376,** 236-238.

Deshmukh SS & Knierim JJ. (2011). Representation of non-spatial and spatial information in the lateral entorhinal cortex. *Front Behav Neurosci* **5,** 69.

Deshmukh SS & Knierim JJ. (2013). Influence of local objects on hippocampal representations: Landmark vectors and memory. *Hippocampus* **23,** 253-267.

Dong LL & Fiete IR. (2024). Grid Cells in Cognition: Mechanisms and Function. *Annu Rev Neurosci* **47,** 345-368.

Douglass JK, Wilkens L, Pantazelou E & Moss F. (1993). Noise enhancement of information transfer in crayfish mechanoreceptors by stochastic resonance. *Nature* **365,** 337-340.

Edvardsen V, Bicanski A & Burgess N. (2020). Navigating with grid and place cells in cluttered environments. *Hippocampus* **30,** 220-232.

Erchova I, Kreck G, Heinemann U & Herz AV. (2004). Dynamics of rat entorhinal cortex layer II and III cells: characteristics of membrane potential resonance at rest predict oscillation properties near threshold. *The Journal of physiology* **560,** 89-110.

Faisal AA, Selen LP & Wolpert DM. (2008). Noise in the nervous system. *Nature reviews Neuroscience* **9,** 292-303.

Fuhs MC & Touretzky DS. (2006). A spin glass model of path integration in rat medial entorhinal cortex. *J Neurosci* **26,** 4266-4276.

Fyhn M, Molden S, Witter MP, Moser EI & Moser MB. (2004). Spatial representation in the entorhinal cortex. *Science* **305,** 1258-1264.

Gardner RJ, Hermansen E, Pachitariu M, Burak Y, Baas NA, Dunn BA, Moser M-B & Moser EI. (2022). Toroidal topology of population activity in grid cells. *Nature***,** 1-6.

Gingl Z, Kiss L & Moss F. (1995). Non-dynamical stochastic resonance: Theory and experiments with white and arbitrarily coloured noise. *EPL (Europhysics Letters)* **29,** 191.

Giocomo LM. (2016). Environmental boundaries as a mechanism for correcting and anchoring spatial maps. *The Journal of physiology* **594,** 6501-6511.

Giocomo LM, Zilli EA, Fransen E & Hasselmo ME. (2007). Temporal frequency of subthreshold oscillations scales with entorhinal grid cell field spacing. *Science* **315,** 1719-1722.

Gluckman BJ, Netoff TI, Neel EJ, Ditto WL, Spano ML & Schiff SJ. (1996). Stochastic Resonance in a Neuronal Network from Mammalian Brain. *Phys Rev Lett* **77,** 4098-4101.

Haas JS & White JA. (2002). Frequency selectivity of layer II stellate cells in the medial entorhinal cortex. *Journal of neurophysiology* **88,** 2422-2429.

Hafting T, Fyhn M, Molden S, Moser MB & Moser EI. (2005). Microstructure of a spatial map in the entorhinal cortex. *Nature* **436,** 801-806.

Hänggi P, Jung P, Zerbe C & Moss F. (1993). Can colored noise improve stochastic resonance? *Journal of Statistical Physics* **70,** 25-47.

Hardcastle K, Ganguli S & Giocomo LM. (2015). Environmental boundaries as an error correction mechanism for grid cells. *Neuron* **86,** 827-839.

Hasselmo ME & Brandon MP. (2012). A model combining oscillations and attractor dynamics for generation of grid cell firing. *Front Neural Circuits* **6,** 30.

Hutcheon B & Yarom Y. (2000). Resonance, oscillation and the intrinsic frequency preferences of neurons. *Trends Neurosci* **23,** 216-222.

Khona M & Fiete IR. (2022). Attractor and integrator networks in the brain. *Nature reviews Neuroscience* **23,** 744-766.

McDonnell MD & Abbott D. (2009). What is stochastic resonance? Definitions, misconceptions, debates, and its relevance to biology. *PLoS Comput Biol* **5,** e1000348.

Mishra P & Narayanan R. (2023). The enigmatic HCN channels: A cellular neurophysiology perspective. *Proteins*.

Mittal D & Narayanan R. (2021). Resonating neurons stabilize heterogeneous grid-cell networks. *Elife* **10**.

Mittal D & Narayanan R. (2022). Heterogeneous stochastic bifurcations explain intrinsic oscillatory patterns in entorhinal cortical stellate cells. *Proc Natl Acad Sci U S A* **119,** e2202962119.

Mittal D & Narayanan R. (2024). Network motifs in cellular neurophysiology. *Trends Neurosci* **47,** 506-521.

Moss F. (1997). Stochastic resonance at the molecular level. *Biophys J* **73,** 2249-2250.

Navratilova Z, Giocomo LM, Fellous JM, Hasselmo ME & McNaughton BL. (2012). Phase precession and variable spatial scaling in a periodic attractor map model of medial entorhinal grid cells with realistic after-spike dynamics. *Hippocampus* **22,** 772-789.

Nozaki D, Mar DJ, Grigg P & Collins JJ. (1999). Effects of colored noise on stochastic resonance in sensory neurons. *Physical review letters* **82,** 2402.

Nozaki D & Yamamoto Y. (1998). Enhancement of stochastic resonance in a FitzHugh-Nagumo neuronal model driven by colored noise. *Physics Letters A* **243,** 281-287.

Pastoll H, Ramsden HL & Nolan MF. (2012). Intrinsic electrophysiological properties of entorhinal cortex stellate cells and their contribution to grid cell firing fields. *Frontiers in neural circuits* **6,** 17.

Pollock E, Desai N, Wei X-x & Balasubramanian V. (2018). Dynamic self-organized error-correction of grid cells by border cells. *arXiv preprint arXiv:180801503*.

Ribrault C, Sekimoto K & Triller A. (2011). From the stochasticity of molecular processes to the variability of synaptic transmission. *Nat Rev Neurosci* **12,** 375-387.

Russell DF, Wilkens LA & Moss F. (1999). Use of behavioural stochastic resonance by paddle fish for feeding. *Nature* **402,** 291-294.

Samsonovich A & McNaughton BL. (1997). Path integration and cognitive mapping in a continuous attractor neural network model. *J Neurosci* **17,** 5900-5920.

Savelli F & Knierim JJ. (2019). Origin and role of path integration in the cognitive representations of the hippocampus: computational insights into open questions. *J Exp Biol* **222**.

Savelli F, Yoganarasimha D & Knierim JJ. (2008). Influence of boundary removal on the spatial representations of the medial entorhinal cortex. *Hippocampus* **18,** 1270-1282.

Simonotto E, Riani M, Seife C, Roberts M, Twitty J & Moss F. (1997). Visual Perception of Stochastic Resonance. *Physical Review Letters* **78,** 1186-1189.

Solstad T, Boccara CN, Kropff E, Moser MB & Moser EI. (2008). Representation of geometric borders in the entorhinal cortex. *Science* **322,** 1865-1868.

Wang R & Kang L. (2022). Multiple bumps can enhance robustness to noise in continuous attractor networks. *PLoS Comput Biol* **18,** e1010547.

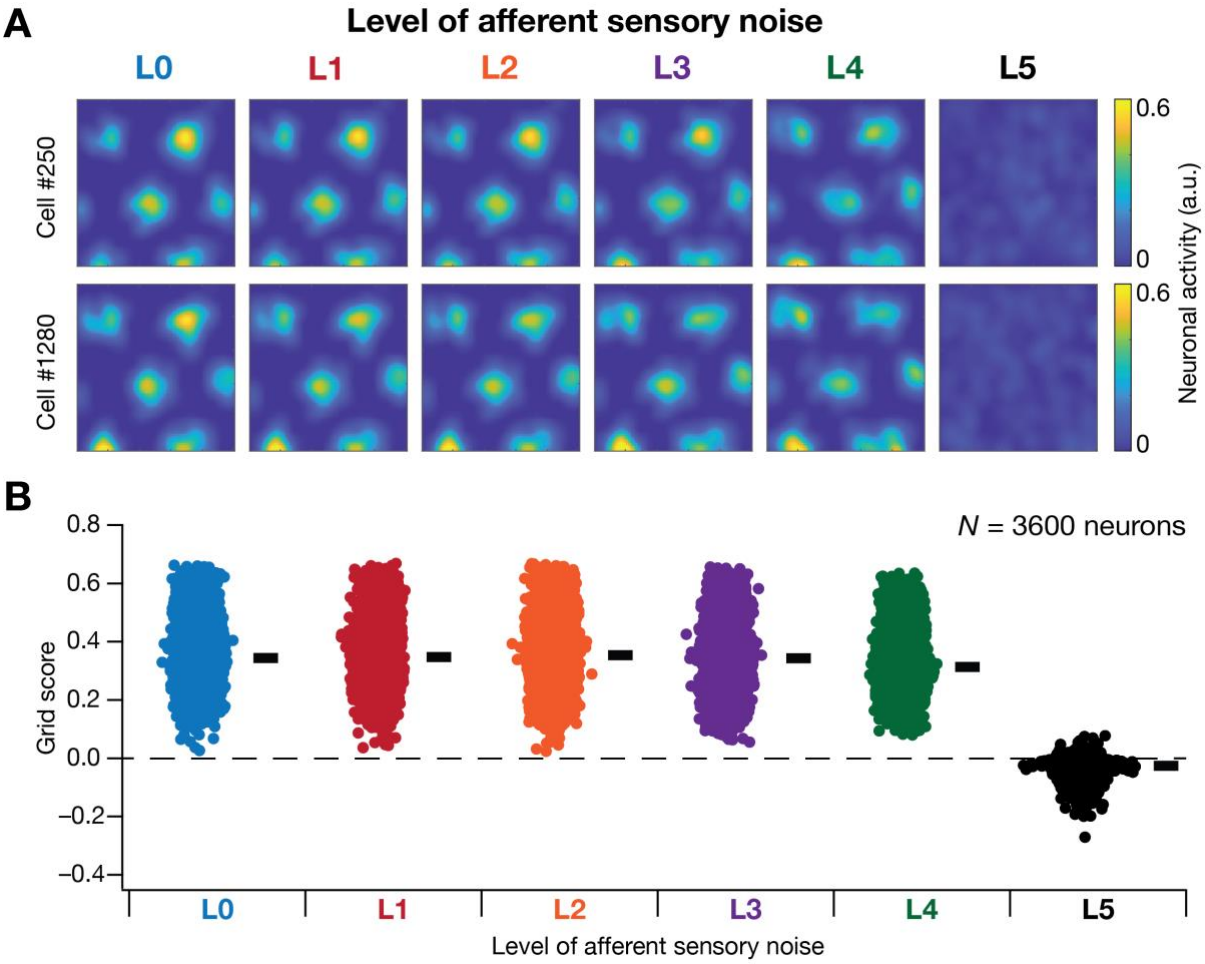

Figure 1. Robustness of grid-patterned firing to the introduction of afferent noise. (*A*) Example spatial rate maps for two representative cells at different levels of noise. The standard deviation of the noise σ_η is provided above each spatial map. The absence of grid-patterned firing may be noted for the map obtained with highest noise level ($\sigma_\eta = 10^{-2}$). (*B*) Bee-swarm plots of the grid score of all 3600 neurons at different levels of noise. The black bar represents the respective median value.

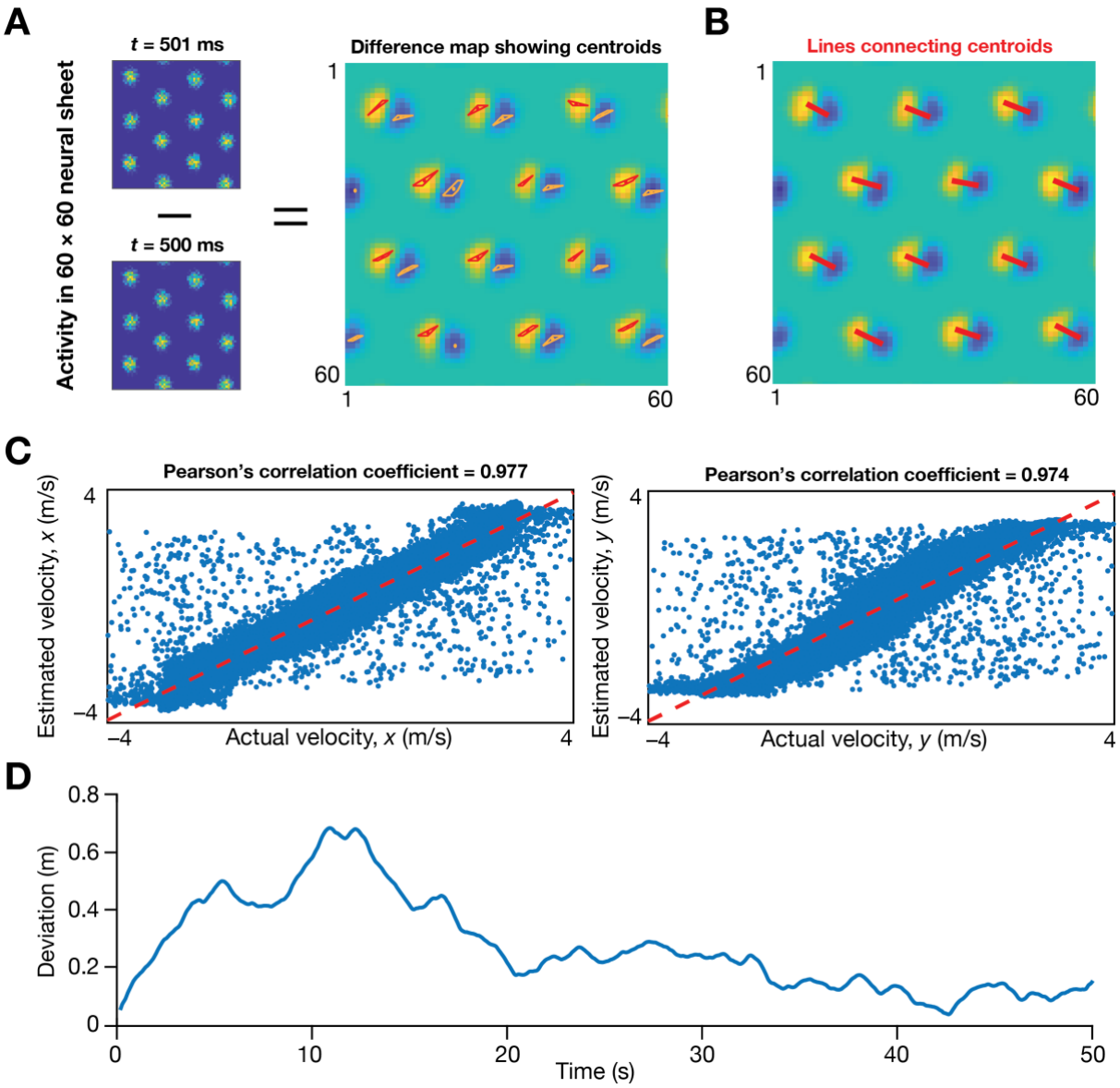

Figure 2. Procedure to compute deviation in position estimate from the network pattern flow velocity. (*A*) Activity difference map at an example timepoint (500 ms) computed as the difference between the activity map at 501 ms and the activity map at 500 ms. The regions in yellow represent the maxima (thus denoting the cells that were more active at 501 ms), while ones in blue represent the minima (cells that were more active at 500 ms). The convex hulls for the maxima are represented in red, while those for the minima are represented in yellow, with the respective centroids of the computed hulls represented as dots. (*B*) The red lines represent the difference between the centroids of the convex hulls of the adjacent maxima and minima. All red lines are averaged to yield the network pattern velocity, providing the magnitude and direction of shift in the network pattern. The magnitude of the average shift represents the mean hull separation. (*C*) Scatter plots representing the relationship between the v_x (left) and v_y (right) components of the estimated *vs.* the actual velocity values computed across all time points. (*D*) Deviation in integrated path, D_{IP}, plotted as a function of time for an example run.

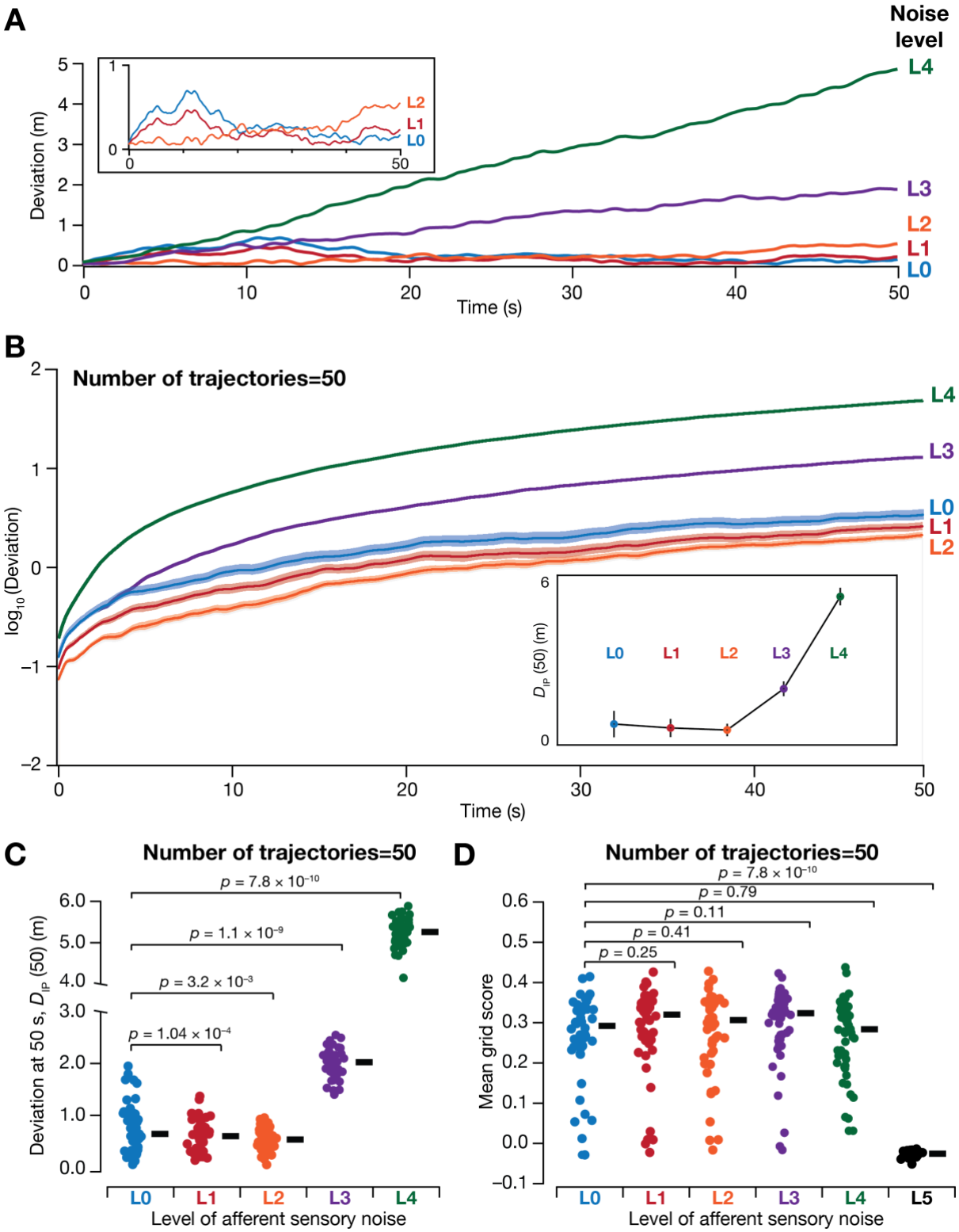

Figure 3. Low levels of afferent noise enhanced position estimates without altering grid scores. (*A*) Example traces of deviation in integrated path, D_{IP}, computed for a single trajectory at different levels of noise (L0–L4). Inset shows the same traces for L0–L2 levels of noise with a zoomed *y*-axis. (*B*) Mean-SEM of D_{IP}, computed across 50 different virtual trajectories, plotted on log scale for different levels of noise (L0–L4). The solid line represents the mean across the 50 trajectories while the shaded region represents the standard error. (*Inset*) D_{IP} value at the 50 s timepoint plotted as a function of noise level. Circles represent the mean across 50 trajectories and the bars represent the standard deviation. (*C*) Beeswarm plots representing D_{IP} value at the 50 s timepoint for 50 different trajectories at different levels of noise. Each circle represents D_{IP} computed from a different trajectory.

The black bars represent the median across the 50 trajectories. p-values show the outcomes of comparison of no-noise measurements with measurements obtained with different levels of noise and were computed using Wilcoxon rank sum test. The Kruskal Wallis test spanning groups across all noise levels yielded a p value of 2.2×10^{-16}. *(C)* Bee-swarm plots representing the mean grid score across the 3600 neurons in the network for each of the 50 different trajectories at different levels of noise. Each circle represents the mean grid score computed from a different trajectory. The black bars represent the median across the 50 trajectories. p-values show the outcomes of comparison of no-noise measurements with measurements obtained with different levels of noise and were computed using Wilcoxon rank sum test. The Kruskal Wallis test spanning groups across all noise levels yielded a p value of 2.2×10^{-16}.

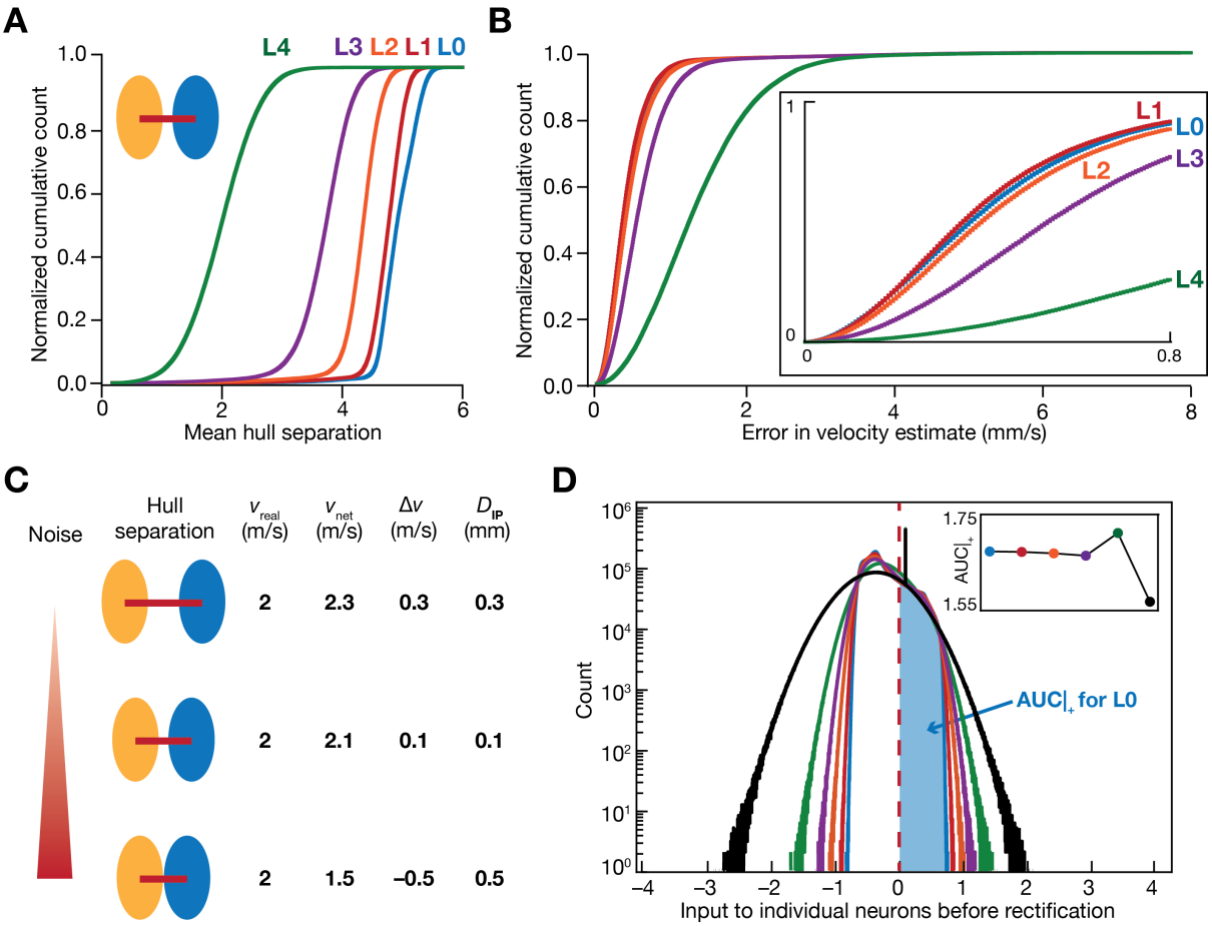

Figure 4. Progressive reduction in mean hull separation with increase in sensory noise variance contributes to dependence of position estimate on sensory noise. (*A*) The yellow and the blue ellipses represent the positive and the negative lobes, respectively, used for computing the network pattern flow velocity (illustrated in Fig. 2*A*–*B*). The magnitude of the red line connecting the centroids of the two lobes is referred to as hull separation. The mean hull separation for each time point is computed by averaging all values of hull separation across every activity bump. The plots represent the distributions of the mean hull separations for different noise levels (L0–L4). (*B*) Distributions of the error in velocity estimate (difference between the velocity estimated using network activity and the actual velocity) for different noise levels. *Inset*, A zoomed version of the distribution spanning lower values of error. (*C*) Model for how increase in noise reduces hull separation, which in turn could contribute to stochastic resonance in $\boldsymbol{D_{IP}}$ observed in Fig. 3*D*. (*D*) Distribution of pre-rectification inputs to the 3600 neurons of the network for a representative trajectory, for different levels of noise. The red line represents the default threshold ($\boldsymbol{\varepsilon}$) in the neural transfer function for the input to manifest as neural activity. The shaded blue region represents the area under the curve (AUC) for the positive part of the distribution for L0 noise level. *Inset*, Area under the curve for the positive part of the distributions for L0–L4 noise levels.

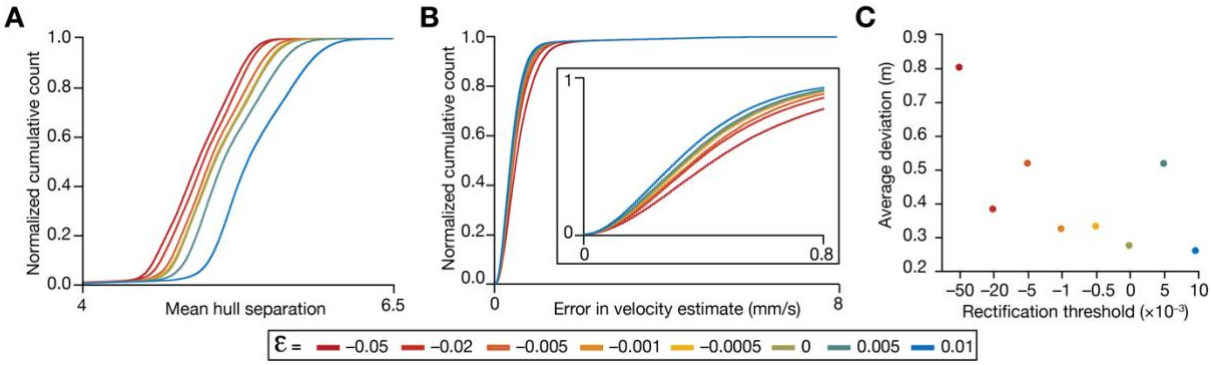

Figure 5. Increase in the rectification threshold in the neural transfer function enhanced mean hull separation and reduced velocity error estimates. (*A*) Distributions of the mean hull separations at different rectification thresholds (introduced by altering ε in the neural transfer function; $f(x) = \max(x, \varepsilon)$). (*B*) Distributions of the error in velocity estimate for different threshold values. *Inset*, Zoomed version of the same plot expanding on the low error region. (*D*) The average deviation (D_{IP}) across time plotted as a function of rectification threshold.

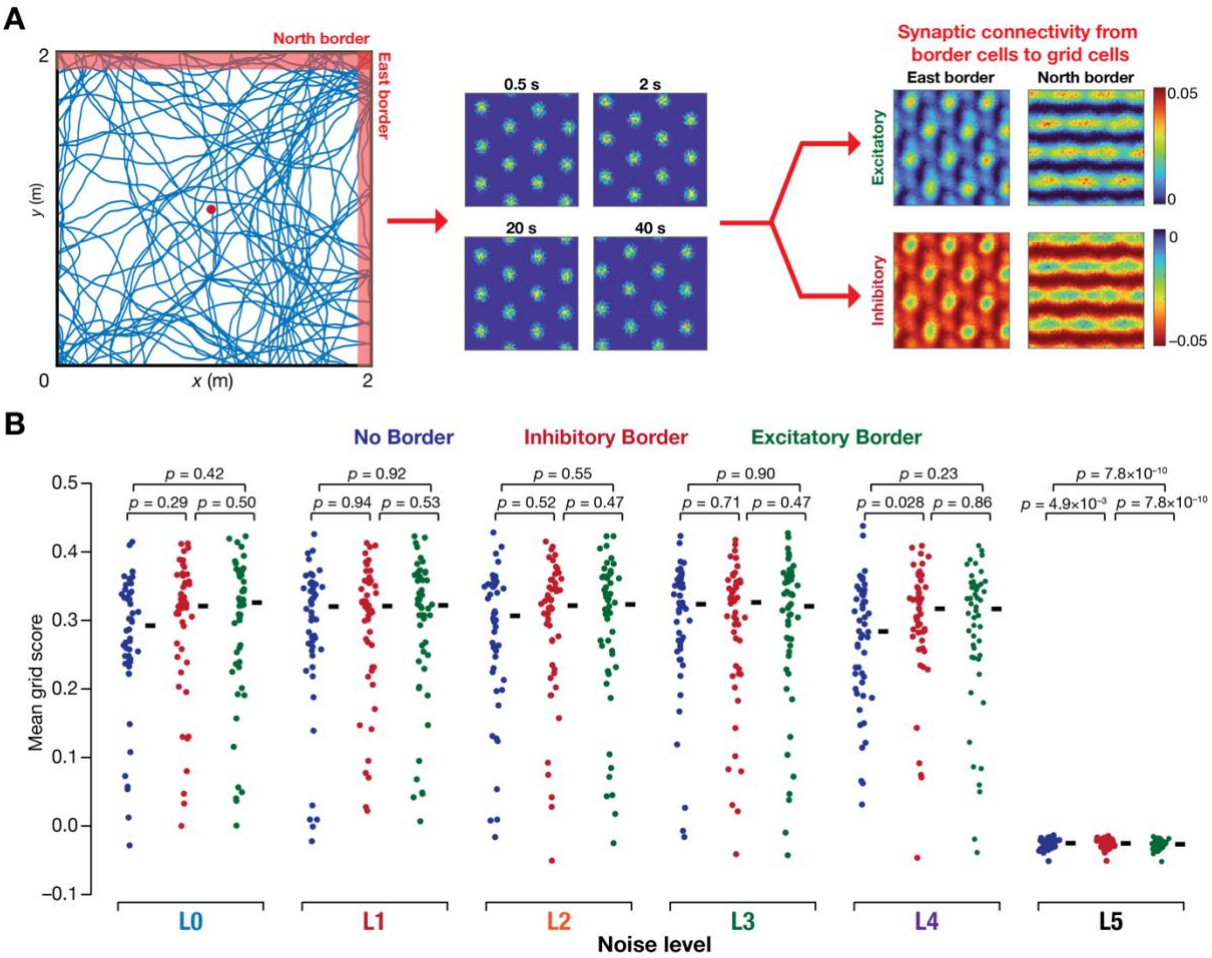

Figure 6. Introduction of border cells, either through excitatory or inhibitory connectivity, yielded modest changes to grid-patterned firing and grid score values. (*A*) Border-to-grid connectivity maps were constructed using results on co-active grid cells from a representative trajectory. *Left*, 2 m × 2 m virtual arena showing the trajectory used to construct the border-to-grid connectivity maps. Our model consisted of two border cells: one that fired along the north border and one that fired along the east border (red shades in the arena). *Middle*, activity map of the grid neural sheet (60×60) at different time points to figure out grid cells that were co-active when border cells were active. *Right*, Connectivity was either excitatory or inhibitory in nature and was defined by co-activity patterns. (*B*) Distribution of mean grid scores (across the 3600 neurons in the network) for the 50 different trajectories, each computed for six different levels of noise (L0–L6). No border results were the same as before. Inhibitory border and excitatory border represent inhibitory and excitatory border-to-grid connectivity patterns, respectively. *p* values are provided for the Wilcoxon rank-sum test. For each level of noise, the *p* values for Kruskal-Wallis test spanning all three border-types were: L0: 0.25; L1: 0.86; L2: 0.73; L3: 0.97; L4: 0.14: L5: 0.50.

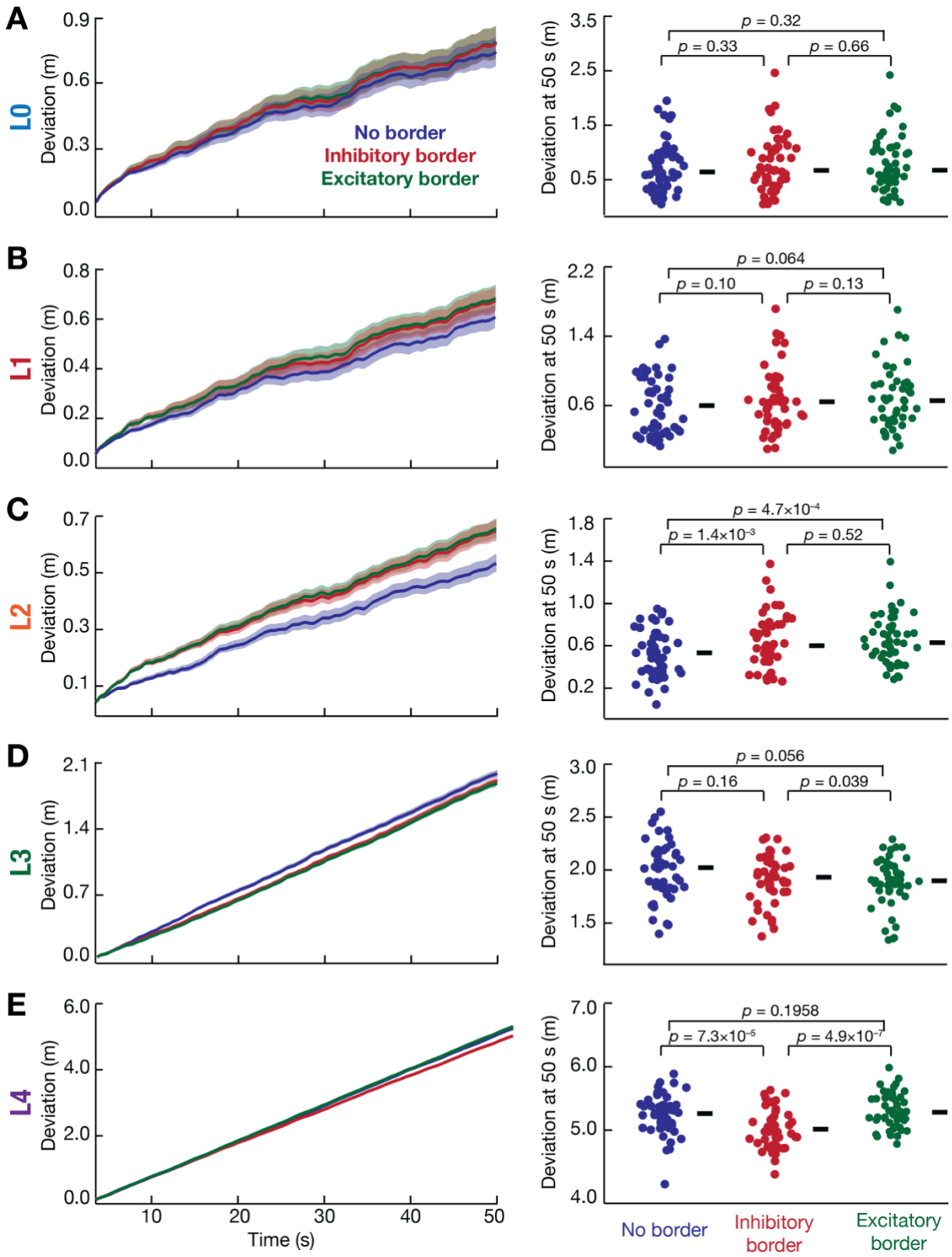

Figure 7. Introduction of border cells, either through excitatory or inhibitory connectivity, yielded modest changes to accuracy of position estimates. (*A–E*) *Left*, Deviation computed across 50 different trajectories as a function of time, for the 3 different types of border inputs (no border, excitatory border, inhibitory border) introduced, for different levels of afferent sensory noise. The solid line represents the mean across the 50 trajectories with the shaded region representing the standard error. *Right*, Bee-swarm plots of the deviation at the 50 s time point for the 50 different trajectories, for 3 types of border input to the network and different levels of sensory noise (L0–L4 spanning panels A–E, respectively). Colors represent the type of border input, with black

bars indicating the median. p values are provided for the Wilcoxon rank-sum test. For each level of noise, the p values for Kruskal-Wallis test spanning all three border-types were: L0: 0.86; L1: 0.60; L2: 3.01×10^{-2}; L3: 0.20; L4: 2.01×10^{-5}.